Pergamon

Int. J. Heat Mass Transfer. Vol. 41, No. 10, pp. 1339–1346, 1998

Printed in Great Britain
0017-9310/98 $19.00+0.00

PII: S0017-9310(97)00200-7

Three-dimensional analysis of heat transfer and thermophoretic particle deposition in OVD process

KI-HYUCK HONG and SHIN-HYOUNG KANG

Department of Mechanical Engineering, Seoul National University, San 56-1, Shinrim-Dong, Kwanak-Ku, Seoul 151-742, Korea

(*Received* 15*th October* 1996)

Abstract—Heat transfer and particle deposition in the OVD process are simply modeled as a buoyant jet flow impinging on a circular target cylinder and numerically analyzed using a finite volume method on the flow, heat transfer and thermophoretic particle deposition over the cylinder. Effects of the three-dimensionality, conjugate heat transfer and longitudinal traversing of the jet on the particle deposition are investigated. The surface temperature, which is the most important value in the whole OVD process, is estimated considering the conjugate heat transfer. As the conductivity of the cylinder decreases, Nusselt number, particle deposition rate and deposition efficiency greatly decrease due to the reduced temperature gradient. Since the increase of the jet traversing speed keeps the surface temperature relatively low, Nusselt number and the particle deposition increase with the traversing speed. © 1998 Elsevier Science Ltd.

1. INTRODUCTION

High quality optical wave guides have been successfully manufactured utilizing the outside vapor deposition (OVD) process. In the process, the silica particles (SiO_2) deposit on the rotating target cylinder due to the thermophoretic force acting on the particle in the direction of decreasing temperature [1]. The particles are produced near the torch through complex chemical reactions in the real process, which is one of the interesting research problems [2]. However, the process was usually simplified and modeled as a high temperature buoyant air jet issuing from the torch and rotating target cylinder. The distributions of velocity, temperature and particle concentration are specified at the exit of the torch.

The thermophoretic particle deposition process wholly depends on the flow and temperature fields around the target cylinder. The target temperature varies both in the axial and circumferential directions when the hot jet impinges on the cylinder and particles deposit, however, most of the studies were carried out assuming two-dimensional flow with the wall temperature specified uniformly. Batchelor and Shen [3], Garg and Jayaraj [4] analyzed the thermophoretic particle deposition on a cylinder in a uniform flow. Kang and Greif [5, 6] considered a plane jet flow to a circular cylinder. Recently, Choi *et al.* [7] made a quasi-three-dimensional numerical analysis for the conjugate heat transfer and thermophoretic particle deposition in the OVD process.

The effects of conjugate heat transfer in the target cylinder as well as three-dimensionality of the flow on the deposition of particle are important for simulation of the real process, however, they were not reported yet. In a previous study [8], we investigated flow and heat transfer when a buoyant circular jet impinges on a circular cylinder. The noticeable difference from the two-dimensional case is that there appear significant axial variation of wall temperature and heat transfer. There is axial flow of lower temperature into the center-plane of the cylinder from the outside of the recirculating region. This results low temperature in the recirculation region and makes the rear part of the cylinder surface cooled.

The inclusion of heat conduction in the target cylinder makes it possible to predict the surface temperature rather than specifying the value as were in the previous studies. Flow, heat transfer and particle deposition over the target cylinder are numerically investigated for different operating conditions, i.e., conductivity of the deposit layer and traversing speed of jet. The effects of jet size, jet exit velocity, rotational speed of the cylinder and variation of properties are also studied.

2. ANALYSIS

2.1. *Governing equations*

Figure 1 shows a schematic diagram of the modeled OVD process consisting of a torch, a jet flow, and a target cylinder, where x and z are the directions of the axes of jet and the circular cylinder, respectively. The gas is air and assumed non-reactive, with particles being formed at the exit of the torch. The continuity, x, y, z momentum, energy equations for the external

NOMENCLATURE

$\mathbf{a}$	contravariant base vector
C	number density [particles cm^{-3}]
c_p	specific heat at constant pressure
D	diameter of the target cylinder
g	square of the Jacobian
g^{ij}	components of the contravariant metric tensor
g_v	acceleration of gravity
Gr	Grashof number, $g_v\beta(T_{jet}-T_{amb})D^3/\nu^2_{amb}$
H	distance between the jet and the center of cylinder
h	heat transfer coefficient, $-k_w(dT/dr)_w/(T_{jet}-T_{amb})$
J	non-dimensional deposition rate, $v_{th,w}C_w/U_{jet}C_{jet}$
K	thermophoretic coefficient
k	thermal conductivity
l_s	length of the separation bubble from the center of cylinder
Nu	Nusselt number, hD/k_{jet}
R	radius of the target cylinder
R_c	characteristic radius of particle jet
R_{jet}	radius of the circular jet
Re	Reynolds number, $U_{jet}D/\nu_{jet}$
T	absolute temperature
U^i	contravariant velocity component
U_{jet}	velocity at the jet exit
v_{th}	thermophoretic velocity, $-K\nu\nabla T/T$
V_{torch}	torch speed [cm/min]
u, v, w	velocity components in x, y and z directions.

Greek symbols

α	thermal diffusivity, $k/\rho c_p$
β	thermal expansion coefficient
η	deposition efficiency
Θ	non-dimensional wall temperature, $(T_{wall}-T_{amb})/(T_{jet}-T_{amb})$
θ	angle
μ	viscosity
ν	kinematic viscosity
ξ^i	curvilinear coordinates [$\xi^1=\xi$, $\xi^2=\eta$, $\xi^3=\zeta$]
ρ	density
Ω	rotation speed of the cylinder.

Subscripts

amb	ambient
jet	value at torch exit
wall	value at the cylinder surface.

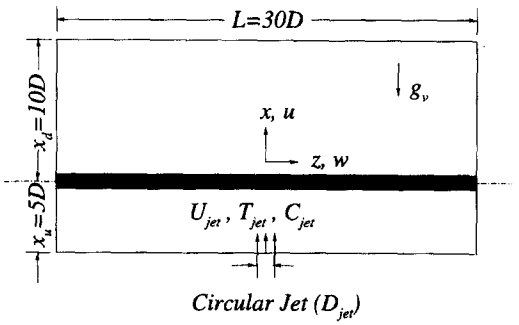

Fig. 1. Schematic diagram of flow configuration ($x-z$ plane).

flow and equation for the conduction in the cylinder are as follows:

$$(\sqrt{g}\rho U^i)_{\xi^i}=0 \tag{1}$$

$$[\sqrt{g}(\rho U^i u-\mu g^{ij}u_{\xi^j})]_{\xi^i}+a^{i1}p_{\xi^i}-\sqrt{g}g_v(\rho-\rho_a)=0 \tag{2}$$

$$[\sqrt{g}(\rho U^i v-\mu g^{ij}v_{\xi^j})]_{\xi^i}+a^{i2}p_{\xi^i}=0 \tag{3}$$

$$[\sqrt{g}(\rho U^i w-\mu g^{ij}w_{\xi^j})]_{\xi^i}+a^{i3}p_{\xi^i}=0 \tag{4}$$

$$[\sqrt{g}(\rho c_p U^i T-kg^{ij}T_{\xi^j})]_{\xi^i}=0 \tag{5}$$

$$\frac{1}{r}\frac{\partial}{\partial r}\left(r\frac{\partial T}{\partial r}\right)+\frac{1}{r}\frac{\partial}{\partial\theta}\left(\frac{1}{r}\frac{\partial T}{\partial\theta}\right)+\frac{\partial}{\partial z}\left(\frac{\partial T}{\partial z}\right)=\frac{\Omega}{\alpha}\frac{\partial T}{\partial\theta}+\frac{V_{torch}}{\alpha}\frac{\partial T}{\partial z} \tag{6}$$

where $\xi^1=\xi$, $\xi^2=\eta$, $\xi^3=\zeta$, $U^i=\mathbf{a}^i\cdot(u\mathbf{i}+v\mathbf{j}+w\mathbf{k})$, $\mathbf{a}^i=\nabla\xi^i$, $g^{ij}=\mathbf{a}^i\cdot\mathbf{a}^j$ and α is thermal diffusivity, Ω and V_{torch} are the rotational speed of cylinder and traversing speed of the torch, respectively. The pressure work, viscous dissipation, and radiation terms are neglected in the energy equation [5–9]. Properties of air such as viscosity μ, specific heat at constant pressure c_p and conductivity k are given as functions of the temperature [6]. The flow is assumed to be steady and laminar throughout the entire domain since the value of Re is less than 1000 [10] and the torch moves along an infinite long cylinder of constant temperature. The conservative equation for the particle concentration is given by

$$[\sqrt{g}U^i_{eff}C]_{\xi^i}=0 \tag{7}$$

neglecting the diffusion by Brownian motion [3, 4]. U^i_{eff} is the sum of the flow and thermophoretic velocities. The thermophoretic velocity is defined as

$$v_{th}=-K\frac{\nu}{T}\nabla T \tag{8}$$

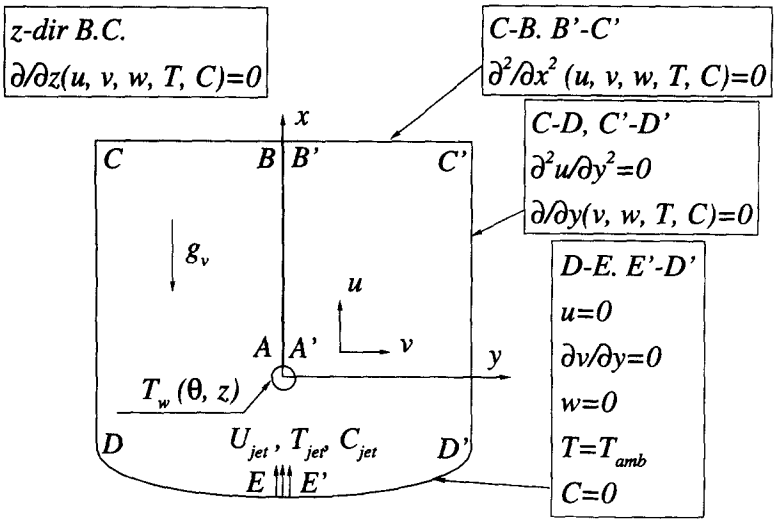

Fig. 2. Computational domain and boundary conditions.

where K is the thermophoretic coefficient. In the present calculation, a constant value of K equal to 0.8 is used [7, 11]. K is usually given as a function of the Knudsen number and the ratio of the thermal conductivity of the gas to that of the particle [1]. The effects of variation of K with temperature and particle size on the deposition are, however, not noticeable as compared with the effects of other parameters [12] for the temperature range of 300–2000 K and sub-micron size particles in the present study.

2.2. *Boundary conditions*

The no-slip condition for the velocity components is given on the surface of the rotating cylinder A-A′ (Fig. 2). On the external boundary C′-D′ and C-D, which locate far from the cylinder, the y derivative of the entrained horizontal velocity component is taken to be zero, $\partial v/\partial y = 0$, and the second derivative of the vertical velocity component is taken to be zero $\partial^2 u/\partial^2 y = 0$, from the assumption of irrotational flow [5]. The flow is assumed to be horizontally entrained at the external upstream boundary on D-E and E′-D′. It was reported that the boundary condition on D-E and E′-D′ did not strongly influence the results [5]. At the far downstream location above the cylinder, B-C and B′-C′, the streamwise second derivatives of the velocity components and the temperature are assumed to be zero. The boundary conditions for all variables in z-direction are $\partial/\partial z = 0$. On E-E′, corresponding to the torch exit, the velocity and temperature are uniform, i.e. $u = U_{jet}$, $v = 0$, and $T = T_{jet}$. The static pressure is zero as a reference value. The particle concentration at the torch exit is specified by the Gaussian distribution [6, 7] as follows:

$$C_{jet}(r) = C_{jet,max} \exp[-\ln 2(r/R_c)^2] \qquad (9)$$

where R_c is the characteristic radius of the particle jet ($R_c/R_{jet} = 0.1$). The concentration on the regions D-E, D′-E′, C-D, and C′-D′ is zero, and boundary condition is not required on A-A′, since the concentration equation is first order.

Equation (6) should be solved simultaneously with the eqns (1)–(5). The temperature field of the external jet flow and the distribution of temperature in the cylinder are solved by an iterative solution method. The surface heat flux obtained from the temperature field of the external flow is used as a boundary condition to solve the conduction heat transfer in the cylinder. And then the surface temperature of the cylinder is again used as a temperature boundary condition for the jet flow. The above procedure is repeated until convergence is attained.

2.3. *Particle deposition rate and efficiency*

The effectiveness of the particle deposition process can be assessed by deposition rate and efficiency. The deposition rate is equal to the normal component of the thermophoretic velocity multiplied by the particle concentration at the wall. The non-dimensional deposition rate J is defined by

$$J = \frac{v_{th,w} C_w}{U_{jet} C_{jet}}. \qquad (10)$$

The concentration at the wall, C_w, is obtained by considering the boundary layer equations [6]. The efficiency of particle deposition is defined as the ratio of the total deposition rate to the incoming particle mass flow rate as follows:

$$\eta = \frac{\int_{-L/2}^{L/2} \int_{-\pi}^{\pi} v_{th,w} C_w R \, d\theta \, dz}{\int_0^{R_{jet}} \int_{-\pi}^{\pi} U_{jet} C_{jet} r \, d\theta \, dr}. \qquad (11)$$

As SiO_2 particles continue to deposit on the target

cylinder, deposited porous layers are formed. The porosity of the deposited layer affects subsequent dehydration and sintering; the period of the processes and the crack of the layers, etc.

2.4. *Numerical procedure*

Since the accurate prediction of local heat transfer on the surface of cylinder, especially near the stagnation point, is of importance, a C-type grid system is adopted. Three different sets of grid system were tested for grid sensitivity for the external jet flow field: $(71 \times 31 \times 21)$, $(91 \times 41 \times 31)$ and $(111 \times 51 \times 41)$ in the ξ, η, ζ directions. The present calculation of the conduction heat transfer in the cylinder is in good agreement with the analytic solution obtained using the Fourier transformation [12]. Grids of $(91 \times 41 \times 31)$ and $(r \times \theta \times z = 51 \times 20 \times 31)$ for the external jet flow and conduction in the cylinder, respectively, show reasonable grid-independent results. Further numerical tests are given in ref. [12].

The pressure is calculated using the SIMPLE algorithm of Patankar [13] with the HYBRID method for the convective terms considering small Reynolds number [5–7] and a non-staggered system is used to solve the equations. A Modified Strongly Implicit (MSI) [14] method is adopted to solve the momentum and energy equations and Conjugate Gradient Solver (CGS) [15] is used for the continuity equation.

3. RESULTS AND DISCUSSION

3.1. *Range of conditions*

The important parameters in the present study are the rotational speed of the cylinder Ω, the radius of cylinder R, the distance between the jet exit and the center of cylinder H, the radius of circular jet R_{jet}, the jet velocity U_{jet} and the jet, air and wall temperatures. Three-dimensional flow, heat transfer and particle deposition are numerically investigated for the range of values of non-dimensional parameter as follows;

$$Re = U_{jet}D/\nu_{jet} = 106, \mathbf{213}, 426, \underline{639}$$

$$Gr/Re^2 = \underline{4.4}, 10, \mathbf{40}, 160$$

$$R_{jet}/R = 0.25, \underline{0.6}, \mathbf{1.2}, 2.4$$

$$H/R = 10.0$$

with fixed values of $R = 1$ cm, $U_{jet} = 4$ m s^{-1}, $T_{jet} = 2000$ K, $T_{amb} = 300$ K. Since the tangential speed of the rotating cylinder is about 0.06 m/s for 60 rpm and very small in comparison with the jet velocity, the effect of the rotation of cylinder on the flow and heat transfer is relatively small as compared with that of other parameters [12, 16]. Hence a non-rotating cylinder is considered hereafter. All of the above values are used in two-dimensional case, however, only the underlined values are used for three-dimensional study. The bold-faced values are the standard values of each parameter when the others are changed.

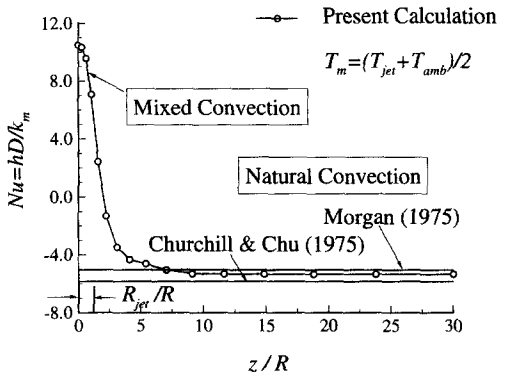

Fig. 3. Comparison of average Nusselt number distribution along the axial direction between the present calculation and correlations.

The additional parameters for the three-dimensional conjugate case are as follows;

$$k_{cylinder} = 0.70, 2.87, \mathbf{7.85}\ \mathrm{W\,m^{-1}K^{-1}}$$

$$V_{torch} = \mathbf{0}, 1, 10\ \mathrm{cm\ min^{-1}}$$

3.2. *Validation of the present calculation*

Since the measured data of the flow and heat transfer for an impinging air jet on a circular cylinder are not available, the present calculation was validated for the two-dimensional case; e.g. a plane jet flow, in the previous studies [5–7].

Circumferentially averaged Nusselt number distribution over the cylinder for the reference values of parameter is shown in Fig. 3. Over the center-plane of cylinder where the hot jet impinges, the jet heats the cylinder by mixed convection. But the surface of the cylinder located far from the jet cools down by the natural convection. Unlike the uniform flow case, there are three characteristic temperatures, i.e. jet temperature, T_{jet} in addition to T_{wall} and T_{amb}. This makes the direct comparison between the heat transfer in the uniform flow and the present calculation difficult. As shown in Fig. 3, however, calculated Nusselt numbers agree well with the available correlations in the natural convection regime. Nusselt numbers in the present study show -5 and $+9\%$ differences as compared with the estimated values of the correlations of Morgan [17], Churchill and Chu [18], respectively. Note that averaged Nusselt number decreases monotonically from the center to the end of the cylinder.

3.3. *Three-dimensional flow and heat transfer characteristics*

When a circular jet impinges on a circular cylinder, the flow and heat transfer characteristics are different from those of the two-dimensional case, especially over the stagnation and recirculation region. They are simulated for the standard values of parameter with specified constant wall temperature;

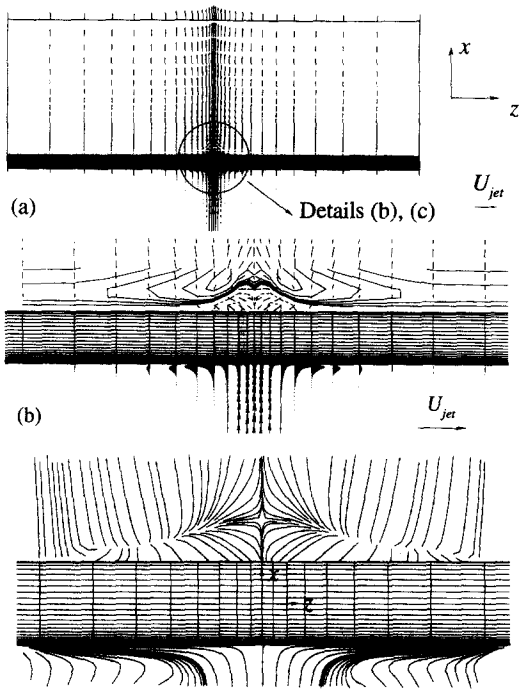

Fig. 4. (a) Velocity vectors, (b) pressure contours, dashed line (-value) and (c) pathlines in the x–z plane ($y = 0$).

$$Re = 213, \quad Gr/Re^2 = 40, \quad R_{jet}/R = 1.2,$$
$$H/R = 10, \quad \Theta = 0.5.$$

Velocity vectors and pathlines in the x–z plane for case of constant wall temperature are plotted in Fig. 4. The axisymmetric buoyant jet effluxing from the torch entrain the ambient cold air with momentum and heat loss. As the jet impinges on the target cylinder, the wall jet spreads in the axial and circumferential directions from the stagnation point shown in Fig. 4(a). Note that there is no axial flow in the two-dimensional plane jet. In the wake region downstream, the streamwise velocity gradually increase due to the buoyancy force. The details of the Fig. 4(a) plotted in Fig. 4(b) show the velocity vectors and isopressure contours. The wall jet in the axial direction of the cylinder has its maximum value around $z/R = 1.2$ and then gradually decreases. The wall jet finally disappears beyond $z/R = 6.0$. The flow pattern in the downstream region of the cylinder can be observed more clearly by pathlines plotted in Fig. 4(c). The flow region of the center-plane of the cylinder can be divided into recirculation and jet wake regions by the saddle point which locates at $x/R = 2.3$. Pathlines in the recirculation region indicate that the outer-flow is induced into the center-plane by the pressure gradient in the axial direction of the cylinder. The recovery of pressure is fast so that the size of separation bubble is small as compared with that of the two-dimensional case.

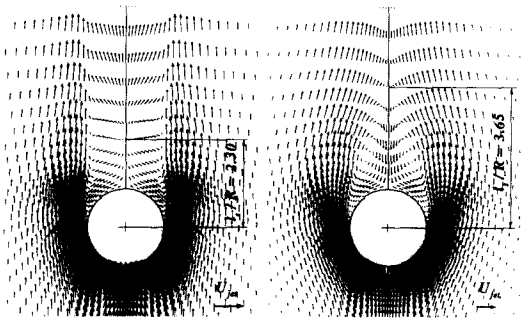

(a) 3-dim. (circular jet) (b) 2-dim. (plane jet)

Fig. 5. Comparison of velocity vectors in the center-plane of the cylinder between 2D and 3D.

Three-dimensional flow on the center-plane of the cylinder is shown in Fig. 5 and compared with the two-dimensional case. From the jet exit up to the stagnation point of the cylinder, the flow patterns of those two cases are almost the same. However, in the recirculation region, Fig. 5(a) indicates that the length of the separation bubble of the three-dimensional case ($l_s/R = 2.3$) is greatly reduced as compared with that of the plane jet case [Fig. 5(b), $l_s/R = 3.65$]. This is due to the axial flow entrainment into the center-plane. The inflow results in recovery of pressure and makes the reverse flow in the recirculation region decrease to $u/U_{jet,max} = -0.13$ (compare -0.52, the value of 2D case).

The flow affects temperature fields as shown in Fig. 6. The value of non-dimensional temperature is 0.5 on the cylinder, 1.0 in the jet core, and 0.0 far from the target. Several isothermal contours completely enclose the cylinder for the plane jet case [Fig. 6(b)], which means the external flow temperature is higher than that of the target all over the wall. For the circular jet case, however, the isothermal contours are partly broken by the axially entrained flow of the cold ambient air over the rear stagnation and recirculation region [Fig. 6(a)]. This results in low-temperature in the recirculation region downstream and makes the surface cooled, although the whole surface is heated

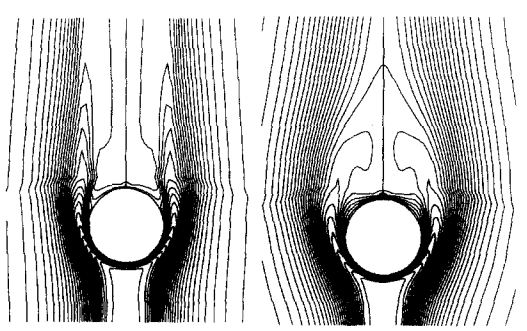

(a) 3-dim. (circular jet) (b) 2-dim. (plane jet)

Fig. 6. Comparison of temperature contours in the center-plane of the cylinder between 2D and 3D.

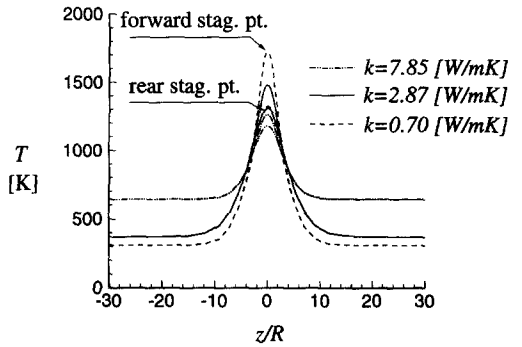

Fig. 7. Effect of thermal conductivity of the cylinder on the distribution of axial surface temperature at the forward and rear stagnation points.

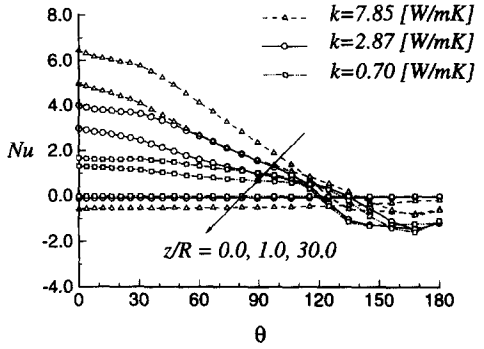

Fig. 8. Effect of thermal conductivity of the cylinder on the distribution of local Nusselt number over the cylinder surface at the different axial locations.

by the recirculating hot flow for the plane jet case. More plane views of the flow and temperature fields at different axial locations are given in refs. [8, 12].

The patterns of the flow and temperature distributions are generally the same for different values of parameters, e.g., the size of the jet, buoyance force and wall temperature [16]. As the size of the jet is larger, skin-friction coefficient and local Nusselt number over the cylinder surface have higher values due to the higher speed and temperature of the jet over the target with the smaller momentum and energy losses of the jet to the ambient air relative to the efflux values. The buoyancy force accelerates the flow so that the speed and temperature of the jet over the target become higher. This results in higher values of skin-friction coefficient and local Nusselt number over the surface. When the wall temperature increases, the skin-friction coefficients increase and local Nusselt numbers decrease due to the higher viscosity and reduced temperature gradient on the wall.

3.4. *Effect of the thermal conductivity of deposit layer*

Since the deposit layer (SiO_2) of low conductivity (compared to the alumina cylinder) is formed over the cylinder surface and the hot circular jet impinges on the cylinder in the real OVD process, the wall temperature is neither uniform nor pre-specified. The thermal conductivities of the porous silica layer (porosity = 0.85) and the fused silica are 0.10 and 2.87 W m^{-1} K^{-1} at 1000 K, respectively [19]. Note that the thermal conductivity of the alumina cylinder is 7.85 W m^{-1} K^{-1}. To investigate the effects of the deposit layer on the flow and heat transfer, the two layers of cylinder should be considered with different thermal conductivities. In the present study, however, the effects are investigated by changing the value of the conductivity of the single-layer cylinder.

Figure 7 shows the axial variation of the surface temperature at the forward and rear stagnation points for three different thermal conductivities of 7.85, 2.87, 0.7. The value of temperatures is the highest at the forward stagnation point and decreases along the axis of the cylinder, however, becomes almost uniform beyond $z/R = 5.0$. The maximum temperature differences over the cylinder are 600, 1100, 1500 K, respectively. Increase of the difference is due to the reduced axial conduction heat transfer for the low conductivity cylinder. Note that circumferential temperature differences also increase, i.e. 100, 200, 400 K, as the thermal conductivity decreases.

From the jet exit to the stagnation point of the cylinder, there are no noticeable differences in the main stream velocity, pressure and temperature distributions for different values of thermal conductivity [12]. However, as shown in Fig. 8, there are remarkable changes in the local Nusselt numbers over the cylinder surface with conductivity even though there are no apparent changes in the pressure and skin-friction coefficients [12]. Note that the heat transfer coefficient is defined based on the jet and ambient temperature difference, not the jet and wall temperature, since the wall temperature is obtained from the solution. Over the center-plane of the cylinder, the temperature difference between the flow and surface decreases with the decrease of thermal conductivity, which results in the increase of thermal boundary layer thickness. This reduces the normal temperature gradient and correspondingly local Nusselt numbers over the surface with the decrease of thermal conductivity.

The circumferentially averaged Nusselt numbers have maximum values at the center-plane of the cylinder, i.e. 2.43, 1.32, 0.45, decrease and become negative along the cylinder as shown in Fig. 9. The figure also indicates the assumption of uniform wall temperature may cause considerable error in the estimation of the thermal field and particle deposition as the thermal conductivity of the layer decreases. At the end of the cylinder, the amount of cooling by natural convection decreases with the decrease of the thermal conductivity due to the small difference between the wall and ambient temperature. Note that the region where particles can deposit becomes narrow as the thermal conductivity decreases.

The magnitude of thermophoretic velocity is almost proportional to the Nusselt number [5, 12]. The particle deposition rate decreases with the decrease of

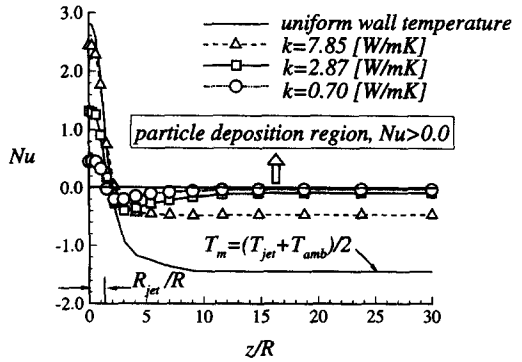

Fig. 9. Effect of thermal conductivity of the cylinder on the axial distribution of circumferentially averaged Nusselt number over the cylinder surface.

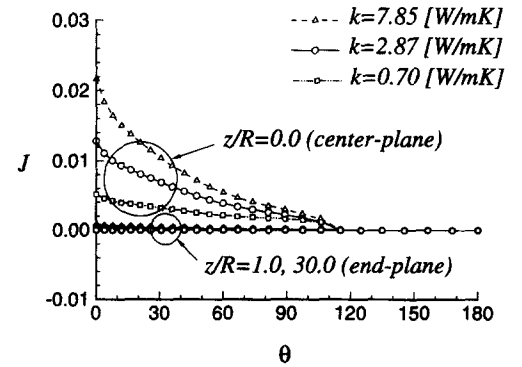

Fig. 10. Effect of thermal conductivity of the cylinder on the distribution of local deposition rate over the cylinder surface at the different axial locations of the cylinder.

thermal conductivity as shown in Fig. 10. Circumferentially averaged deposition rate shown in Fig. 11 indicates that most of injected particles deposit over the center-plane of the cylinder, $-1.5 < z/R < 1.5$. As thermal conductivity of the cylinder decreases, the averaged deposition rate and efficiency decrease due to the increase of the surface temperature [12].

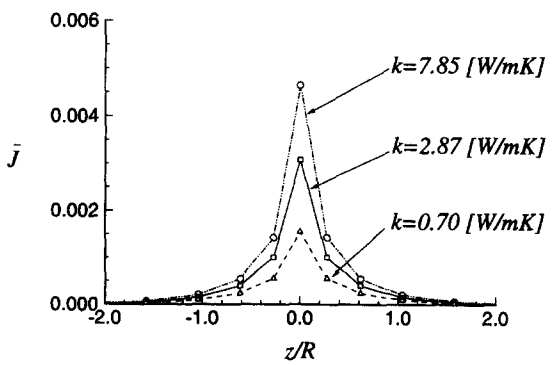

Fig. 11. Effect of thermal conductivity of the cylinder on the axial distribution of circumferentially averaged deposition rate over the cylinder surface.

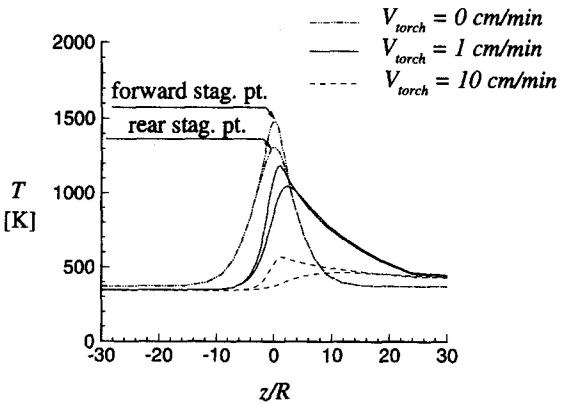

Fig. 12. Effect of traversing speed of torch on the distribution of axial surface temperature at the forward and rear stagnation points.

3.5. *Effects of traversing speed of torch*

Traversing of the torch is necessary for uniform deposition and control of the refractive index of the layers. Calculation of heat transfer and deposition are carried out for three speeds of 0, 1, 10 cm min^{-1}. The coordinate is moving with the torch and the cold cylinder is coming into relative to the torch in the calculation model.

Figure 12 shows the axial temperature distributions at the forward and rear stagnation points for the standard conditions and thermal conductivity of the fused silica at 1000 K, 2.87 W m^{-1} K^{-1}. The higher torch speed results in the lower cylinder surface temperatures as expected. Note that the surface temperatures of the forward stagnation point in the center-plane of the cylinder are 1500, 1200, 600 K, respectively as the torch speed increases as 0, 1, 10 cm min^{-1}. The remarkable changes in the surface temperature indicate that torch traversing is one of the most affective tool of control in the optimization of the particle deposition process. Though the low surface temperature makes the thermal conductivity of gas smaller, thickness of thermal boundary layer reduces and the temperature gradient increases. This makes the local Nusselt numbers over the cylinder surface increase with the traversing speed of the cylinder. Note also that the temperature distributions are not symmetric with respect to the center-plane and the highest temperature locate a little downstream of the cylinder.

Circumferentially averaged deposition rate shown in Fig. 13 indicates that the averaged deposition rate increases as the traversing speed of the torch increases; 0, 1, 10 cm min^{-1}. The increase is mainly due to the decrease of the surface temperature. Deposition efficiency also increases with the torch speed; 0.21, 0.38, 0.45. If the torch speed is too high, the cylinder temperature becomes so low that the porosity of the deposited layer can be large and brittle in the real OVD process.

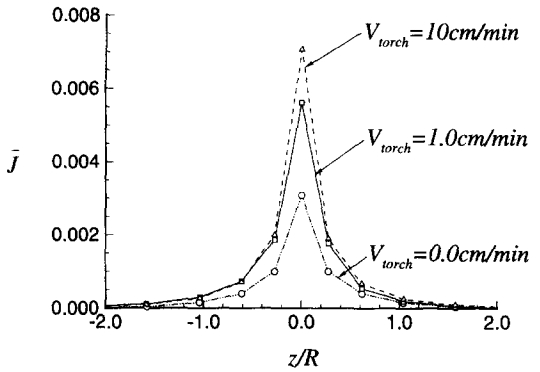

Fig. 13. Effect of traversing speed of torch on the axial distribution of circumferentially averaged deposition rate over the cylinder surface.

4. CONCLUSIONS

The flow, heat transfer and particle deposition in the OVD process are numerically simulated. The process is modeled as a buoyant air jet impinging on a cold circular cylinder with the specified particle distribution. The values of parameters are changed with the reference values of $R = 1$ cm, $R_{jet} = 1.2$ cm, $H = 10.0$ cm, $U_{jet} = 4$ m s^{-1}, $T_{jet} = 2000$ K, $T_{amb} = 300$ K. The following conclusions are drawn from the present parametric study.

(1) In the center-plane of the cylinder, three-dimensional flow is different from two-dimensional case. In the recirculation region, the length of the separation bubble of the three-dimensional case is greatly reduced as compared with that of the plane jet case. This is due to the axial flow-entrainment into the center-plane from the outside by the pressure gradient. The flow results in low-temperature in the recirculation region downstream and makes the target surface cooled, although the whole surface is heated by the recirculating hot flow for the plane jet case.

(2) Analysis of conjugate heat transfer makes it possible to estimate actual thermal field of the process around the target cylinder by calculating the surface temperature rather than specifying the value. The region where particles deposit becomes narrow as thermal conductivity of the deposit layer becomes small and most of injected particles deposit over the center-plane of the cylinder. Deposition rate and efficiency decrease with thermal conductivity due to the increase of the target surface temperature.

(3) Deposition rate increases as the traversing speed of the torch increases since the higher torch speed results in lower cylinder surface temperatures. Deposition efficiency also increases with the increase of traversing speed.

Acknowledgement—The authors are grateful to Prof. M. Choi for helpful discussions and suggestions.

REFERENCES

1. Talbot, L., Cheng, R. K., Schefer, R. W. and Willis, D. R., Thermophoresis of particles in a heated boundary layer. *Journal of Fluid Mechanics*, 1980, **101**(4), 737–758.
2. Tsai, H. C. and Greif, R., Thermophoretic transport for a three-dimensional reacting flow impinging on a disk with burner misalignment. *Journal of Material Processing & Manufacturing Science*, 1995, (3), 217–242.
3. Batchelor, G. K. and Shen, C., Thermophoretic deposition of particles in gas flowing over cold surfaces. *Journal of Colloid Interface Science*, 1985, **107**(1), 21–37.
4. Garg, V. K. and Jayaraj, S., Thermophoretic deposition over a cylinder, *International Journal of Engineering Fluid Mechanics*, 1990, **3**(2), 175–196.
5. Kang, S. H. and Greif, R., Flow and heat transfer to a circular cylinder with a hot impinging air jet. *International Journal of Heat and Mass Transfer*, 1992, **35**, 2173–2183.
6. Kang, S. H. and Greif, R., Thermophoretic transport in the outside vapor deposition process. *International Journal of Heat and Mass Transfer*, 1993, **36**, 1007–1018.
7. Choi, M., Song, Y. and Kang, S. H., Conjugate heat transfer and particle transport in outside vapor deposition process. *Numerical Heat Transfer*, 1995, **28**, 39–54.
8. Kang, S. H. and Hong, K. H., Three-dimensional flow and heat transfer to a circular cylinder with a hot circular impinging air jet. *Proceedings of ISTP-9 in Thermal-fluids Engineering*, Vol. 2, Singapore, 1996, pp. 801–806.
9. Lee, K. H., Analysis of radiative heat transfer and particle deposition using the finite volume method in the non-orthogonal coordinate system. Ph.D. thesis, Seoul National University, Seoul, 1995.
10. Tennekes, H. and Lumley, J. L. *A First Course in Turbulence*, MIT Press Cambridge, MA, 1972.
11. Bautista, J. R., Walker, K. L. and Aktins, R. M., Modeling heat and mass transfer in optical waveguide manufacture. *Chemical Engineering Progress*, 1990, 47–52.
12. Hong, K. H., A study on the heat transfer and themophoretic particle deposition over a circular cylinder. Ph.D. thesis, Seoul National University, Seoul, 1996.
13. Patankar, S. V., *Numerical Heat Transfer and Fluid Flow*, Hemisphere, New York, 1980.
14. Zedan, M. and Schneider, G. E., A three-dimensional modified strongly implicit procedure for heat conduction. *AIAA Journal*, 1983, **21**(2), 295–303.
15. Press, W. H., Teukolsky, S. A., Vetterling, W. T. and Flannery, B. P., *Numerical Recipe*, Cambridge Press, New York, 1992.
16. Hong, K. H. and Kang, S. H., Three-dimensional flow characteristics and heat transfer to a circular cylinder with a hot circular impinging air jet. *Transactions of the KSME, B*, 1997, **21**(2), 285–293.
17. Morgan, V. T., The overall convection heat transfer from smooth circular cylinders. *Advances in Heat Transfer*, Vol. 11, Academic Press, New York, 1975, pp. 199–264.
18. Churchill, S. W. and Chu, H. H. S., Correlating equations for laminar and turbulent free convection from a horizontal cylinder, *International Journal of Heat and Mass Transfer*, 1975, **18**, 1049–1053.
19. Incropera, F. P. and Dewitt, D. P., *Introduction to Heat Transfer*, 2nd Edn, Appendix A, Wiley, New York, 1990.